Designing steep, sharp patterns on uniformly ion-bombarded surfaces

Joy C. Perkinson[a], Michael J. Aziz[a], Michael P. Brenner[a], and Miranda Holmes-Cerfon[b,1]

[a]Harvard School of Engineering and Applied Sciences, Harvard University, Cambridge, MA 02138; and [b]Courant Institute of Mathematical Sciences, New York University, New York, NY 10012

Edited by Susan N. Coppersmith, University of Wisconsin, Madison, WI, and approved August 9, 2016 (received for review June 8, 2016)

We propose and experimentally test a method to fabricate patterns of steep, sharp features on surfaces, by exploiting the nonlinear dynamics of uniformly ion-bombarded surfaces. We show via theory, simulation, and experiment that the steepest parts of the surface evolve as one-dimensional curves that move in the normal direction at constant velocity. The curves are a special solution to the nonlinear equations that arises spontaneously whenever the initial patterning on the surface contains slopes larger than a critical value; mathematically they are traveling waves (shocks) that have the special property of being undercompressive. We derive the evolution equation for the curves by considering long-wavelength perturbations to the one-dimensional traveling wave, using the unusual boundary conditions required for an undercompressive shock, and we show this equation accurately describes the evolution of shapes on surfaces, both in simulations and in experiments. Because evolving a collection of one-dimensional curves is fast, this equation gives a computationally efficient and intuitive method for solving the inverse problem of finding the initial surface so the evolution leads to a desired target pattern. We illustrate this method by solving for the initial surface that will produce a lattice of diamonds connected by steep, sharp ridges, and we experimentally demonstrate the evolution of the initial surface into the target pattern.

ion bombardment | steep structure design | simulations | FIB | shock wave

Fabricating steep, sharp features with desired morphologies on surfaces is a major challenge of materials science. Certain methods are available by direct engraving, such as focused ion beam (FIB) or lithography (1–4), but these require enormous time and energy. A promising method to efficiently make patterns on a large scale by exploiting dynamics is to erode a surface with uniform ion bombardment (5–9). A flat surface can become unstable and develop features such as quantum dots or hexagonal patterns (10–17). Such spontaneous pattern growth could spawn high-throughput methods to manufacture periodic metamaterials such as optical antenna arrays (18) and the split ring resonators used in negative refractive index materials and optical cloaking (19).

However, because linear instabilities are neither small enough nor amenable enough to control, interest has recently turned to the potential for nonlinear dynamics to create even steeper, sharper features (20). Large-amplitude, steep structures are of interest for 3D engineering applications such as micromechanics, microprocessor integration, data storage, and photonic band gap waveguides. They are also of interest in atom probe tomography, which uses samples frequently created by FIB ion irradiation (21) and which is strongly influenced by the geometry of the steep-walled final samples (22). Experiments and simulations have shown that knife-edge-like ridges, varying on scales at least an order of magnitude smaller than those accessible to linear instabilities, can arise spontaneously on uniformly bombarded surfaces, provided the initial surface contains slopes beyond a critical value (23, 24). This demonstration suggests that one may be able to create steep, sharp features by first prepatterning a surface on the macroscale—something that is relatively easy to achieve—and then bombarding it uniformly to let even steeper, sharper features form spontaneously.

In this paper we propose a theory to design patterns on a surface using their nonlinear dynamics, and we validate our approach experimentally. We argue that there is a dynamical regime where the full nonlinear dynamics can be approximated by evolving a collection of one-dimensional curves at constant speed in the normal direction, and we show this model accurately describes the experimental behavior of steep-walled pits propagating under uniform ion irradiation approximated via FIB rastering. This model can be used to solve the inverse problem of determining the initial surface pattern that will evolve under uniform ion bombardment to a desired target pattern, and as a demonstration we numerically design and experimentally create a lattice where the scale of the lattice pattern is many times smaller than the scale of the initial patterning.

Our model has several advantages over a direct numerical simulation of the nonlinear equations for surface evolution. First, it can rapidly determine how a given initial condition will evolve, for example by directly evolving the curves or using level set methods (25, 26), so the inverse problem can also be solved efficiently, for example using Monte-Carlo methods. Second, the full nonlinear equations require quantitative information about the macroscopic effects of uniform ion bombardment, such as the yield function (atoms ejected per incident ion as a function of angle of incidence) and the magnitude and type of smoothing physics, and this information is not always known or easy to obtain (27, 28). Our model requires knowing only one material-dependent parameter that can be measured through simple experiments, so measuring the full yield function and smoothing physics is unnecessary. Finally, this

Significance

Large-amplitude, steep structures are of interest for a variety of applications from micromechanics to data storage. Many such structures must be manufactured via effort-intensive direct engraving. Here, we present and experimentally test a method for designing simple structures that will evolve into a desired steep structure under uniform ion irradiation. This process is based on the mathematics of shock waves, a theory originally developed to understand fluids and gases. We show that the dynamics of uniformly bombarded surfaces are controlled by special, so-called undercompressive shocks, which manifest as steep parts of the surface that arise spontaneously and move predictably. Their evolution equation requires only one parameter that is easily measured. The proposed process is scalable with promise for high-throughput manufacturing.

Author contributions: J.C.P., M.J.A., M.P.B., and M.H.-C. designed research; J.C.P. and M.H.-C. performed research; J.C.P. performed focused ion beam/SEM experiments; M.H.-C. performed simulations; M.H.-C. contributed new reagents/analytic tools; J.C.P. and M.H.-C. analyzed data; and J.C.P. and M.H.-C. wrote the paper.

The authors declare no conflict of interest.

This article is a PNAS Direct Submission.

See Commentary on page 11384.

[1]To whom correspondence should be addressed. Email: holmes@cims.nyu.edu.

This article contains supporting information online at www.pnas.org/lookup/suppl/doi:10.1073/pnas.1609315113/-/DCSupplemental.

method is intuitive, so an approximate guess for the initial pattern can be made without any sophisticated numerical techniques.

Results and Discussion

Evolving an Initial Condition to Produce a Target Morphology. We begin by performing numerical simulations of the fully nonlinear, 2D equations for the evolution of the surface height $h(x,y,t)$ under uniform ion bombardment, commonly described by the Sigmund theory of sputter erosion (6). When the surface slope varies over length scales much larger than the lateral scale over which an ion deposits its kinetic energy, the sputter integral can be expanded to yield the following nonlinear partial differential equation (20, 29):

$$h_t + R(b) + B_0 \nabla \cdot \left(\frac{1}{\sqrt{1+b^2}} \nabla \kappa \right) = 0. \quad [1]$$

The first-order term $R(b)$ is the average velocity of erosion of the surface as a function of its slope $b = |\nabla h|$ (or equivalently the angle of the incoming ion beam). The fourth-order term with magnitude B_0 is a function of the surface curvature $\kappa = \nabla \cdot ((1+b^2)^{-1/2} \nabla h)$, which models additional smoothing effects such as Mullins–Herring surface diffusion (30, 31) or ion-enhanced viscous flow confined to a thin surface layer (32). Eq. **1** can also include second-order (curvature) terms (7, 33), but we neglect these because the nonlinear dynamics we wish to model can only occur when these are small (24).

The erosion function $R(b)$ is related to the sputter yield $Y(b)$ by a constant of proportionality that changes its units from [atoms out/ions in] to [length/time]. This constant, as well as steep feature propagation speed, vary with ion flux. Therefore, whereas we measure simulation progress in unitless simulation time, it is more informative to track experimental progress with area dose, a measure of ion fluence delivered per area reckoned in a plane parallel to the average surface. When ion flux is held constant, area dose is proportional to simulation time.

We numerically simulate Eq. **1** using the erosion function for 30-keV Ga^+ on Si (*Materials and Methods*) and estimate length scales for this material combination. Fig. 1 *A–C* shows simulations that begin with a periodic array of shapes punched out in the surface. The shapes are initially 2.5 μm apart (centers 5 μm apart) and are steep at their boundaries with nearly zero slope elsewhere. As the surface evolves, the steep regions remain steep whereas their location changes with time. Eventually the steep regions collide and form ridges that are even steeper, with widths of ≈100 nm. The resulting pattern is a lattice of diamonds connected by steep, narrow ridges.

These ridges were shown in ref. 24 to be a special solution to Eq. **1** that arises whenever steep regions propagating in opposite directions collide. The steepness and radius of curvature of this solution were shown to be fixed numbers that depend on the material, ion, and energy via $R(b)$, and we expect that certain materials can achieve much smaller length scales (23). Because identical ridges arise spontaneously, they are a useful structure to consider for patterns because they are not sensitive to the initial condition.

To show that we can form a similar lattice of knife-edge ridges experimentally, we use FIB to mill four pits matching the initial shape used in simulations and then irradiate under repeated boustrophedonic FIB rastering, delivering a low dose on each pass to approximate uniform irradiation, as described in *Materials and Methods*. Due to discrepancies in pit wall propagation speed (*Supporting Information*, *Speed Calculations*), we milled the initial pits with centers 4.4 μm apart—closer than in simulations. Irradiation continued until the pits impinged (Fig. 1 *D* and *E*). The resulting structure is close to that designed through our method and predicted by the simulations, successfully demonstrating the formation of knife-edge ridges under uniform ion irradiation. One difference from the simulations worth pointing out is that when pits evolved within 200 nm of each other the pit rim closest to the adjacent pit accelerated and "reached out" to the adjacent pits. These behaviors caused impingement to occur both sooner than expected and over a smaller length of the rim. Bombardment was

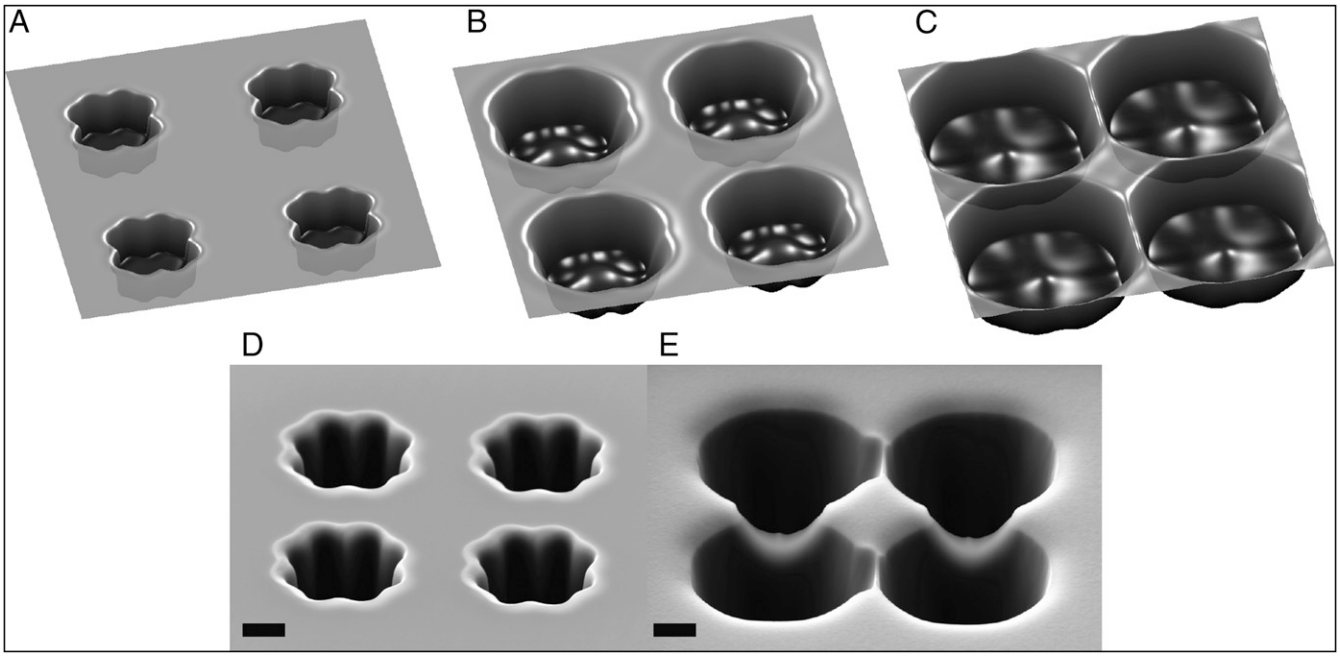

Fig. 1. (*A–C*) Numerical simulation of surface height evolution under uniform ion bombardment (Eq. **1**), at area doses 0 nC/μm^2, 3 nC/μm^2, and 6 nC/μm^2 (simulation times 0, 0.8, and 1.6) Pits initially spaced $O(1)\mu$m apart collide and form ridges with widths $O(100)$ nm. By changing the initial pattern one can create a large variety of patterns made of these steep, sharp ridges. (*D*) SEM image of the fabricated initial condition predicted to evolve into knife-edge ridges, and (*E*) the knife-edge ridges formed after ion irradiation in the FIB, both imaged at 54° off-normal. (Scale bars, 1 μm.)

continued after this impingement to extend the lateral dimensions of the knife edges, and so the knife edge evolved into a curved ridge. Indeed, our simulations show that if bombardment continues beyond the moment of impingement, the knife-edge ridges may evolve into the curved shaped similar to those observed in experiment (Fig. S1).

One-Dimensional Curve Evolution Equations. We designed the pattern of ridges by solving an inverse problem for the initial conditions, and we now explain these calculations. The basic observation is that we can draw a curve through the steepest parts of the surface at every time step and watch the curve evolve in time. Our goal is to derive an evolution equation for the curve using only the curve's intrinsic, one-dimensional geometry, and not any information away from the region of high gradient.

To look for such an equation we recall the theory developed in ref. 23. This theory showed that Eq. **1** has a particular traveling wave solution for the slope that is invariant in one horizontal dimension, that is, of the form $h_x = s(x-ct)$, that acts as an attractor for the dynamics: If a surface is patterned initially to have slopes above a critical value, then the surface steepens and locally evolves to that traveling wave. This wave is called undercompressive in the mathematical literature (34–36) because it has the nonclassical property that information can propagate away from it. In our system it is identifiable because it connects a steep region with constant slope $b_0 = s(-\infty)$ to a flat region with slope $0 = s(\infty)$, and it propagates at constant speed $c = (R(b_0) - R(0))/(b_0 - 0)$, where the constants b_0, c depend on the material, ion, and energy via $R(b)$ but not on the initial condition. When we extract the slope and speed in the simulations of shapes such as in Fig. 1 we find that they are close to b_0, c, suggesting that the surface slope can be locally approximated as a collection of undercompressive traveling waves with slowly varying phase shifts in the transverse direction.

To understand how this collection evolves we consider two different theories. Theory 1 simply advects curves in the normal direction with speed c. If the curve is parameterized by α as $q(\alpha,t) = (x(\alpha,t), y(\alpha,t))$, it evolves according to

$$\frac{dq}{dt} = c\hat{n}, \qquad [2]$$

where $\hat{n} = \frac{\partial q}{\partial \alpha}^{\perp} / \left|\frac{\partial q}{\partial \alpha}\right|$ is the unit normal to the curve. This theory requires only one parameter, the wave speed c, which can be measured by simple experiments. For example, one can engrave a circular pit and measure the rate of change of its radius, as in ref. 24. Theory 1 is a natural heuristic and is expected to be valid when the steep parts of the surface form a curve that is nearly straight, so it can be treated locally as a one-dimensional traveling wave.

Theory 2 seeks to describe the evolution of transverse perturbations to a one-dimensional traveling wave, by looking for an asymptotically consistent solution to the nonlinear, 2D equations. We start by looking for a solution whose slope has the form

$$h_x = s(x - ct + \psi(y,t)) + \epsilon u(x-ct, y, t) + O(\epsilon^2). \qquad [3]$$

We assume the scalings $\partial_y \sim O(\epsilon^{1/2})$, $\partial_t \sim O(\epsilon)$, with $\epsilon \ll 1$. We substitute this ansatz into the x-derivative of Eq. **1** and perform a multiscale asymptotic expansion (37). At leading order is the equation for s, which is satisfied by construction. The $O(\epsilon)$ equation is

$$u_t + \mathcal{L}u = a_1(s)\psi_t + a_2(s)\psi_y^2 + a_3(s)\psi_{yy} + a_4(s)\psi_{yyyy}, \qquad [4]$$

where $a_i(s)$ are functions of the traveling wave (Eqs. **S5**–**S8**) and the linear operator $\mathcal{L}$ is

$$\mathcal{L}u = \partial_\eta((R' - c)u) + B_0\left[\partial^2\eta(f_d\partial_\eta^2(sf)u) + \partial_\eta^2\left(f\partial_\eta^2\left(\left(\frac{1}{2}f_d s^2 + fs\right)u\right)\right)\right]. \qquad [5]$$

We write $\eta = x - ct$, $f(b) = (1+b^2)^{-1/2}$, $f_d(b) = \frac{d}{db}f(b)$, and all functions are evaluated at $s(\eta)$. We have included the term proportional to ψ_{yyyy} from the $O(\epsilon^2)$ equation because it is sometimes required to smooth (*Supporting Information*, *Which Terms to Include in Theory 2?*).

The left-hand side of Eq. **4** depends only on the fast variables η, t, so we can integrate over these to derive a solvability condition. Suppose there is a function $\pi(\eta)$ such that $\mathcal{L}^*\pi = 0$, where $\mathcal{L}^*$ is the adjoint of $\mathcal{L}$ with respect to the L_2 -inner product $\langle\cdot,\cdot\rangle$ [i.e., it satisfies $\int_x u(\mathcal{L}v)dx = \int_x(\mathcal{L}^*u)v dx$ for all u, v with the appropriate boundary conditions]. Taking the inner product with Eq. **4** and requiring u to be bounded shows that $\langle \pi, RHS\rangle = 0$, where RHS is the right-hand side of the equation. Therefore, the phase will evolve on the slow timescale as

$$\psi_t + c_2\psi_y^2 + c_3\psi_{yy} + c_4\psi_{yyyy} = 0, \qquad [6]$$

where $c_i = \langle \pi, a_i(s)\rangle / \langle \pi, a_1(s)\rangle$.

To find π requires solving $\mathcal{L}^*\pi = 0$ with the appropriate boundary conditions, which are $\pi(-\infty) = 0$, $\pi(\infty) = 1$ for the undercompressive traveling wave (35, 38–40). Using these one can compute π numerically, and then the constants can be found by numerical integration. The condition of decay at $-\infty$ is unusual and is what makes this multiscale analysis novel. The condition arises to control information that can propagate away from the traveling wave on its undercompressive side (*Supporting Information*, *Boundary Conditions for the Undercompressive Wave*).

Eq. **6** forms the basis of Theory 2. It demonstrates rigorously that the nonlinear dynamics of an ion-bombarded surface can be approximated (for long-wavelength pertubations) as the evolution of a collection of curves on the surface, each one propagating at constant speed c in a certain direction and changing shape about this direction according to Eq. **6**. The theory requires four parameters: c_2, c_3, c_4, and c. These can be calculated numerically if the erosion rate $R(b)$ and the magnitude of the fourth-order term B_0 are known for a given material. If they are not known, they could be extracted from experiments that measure the evolution of different shapes.

Note that Theory 2 considers perturbations about a horizontal reference line, so it relies on a particular coordinate system. Theory 1, however, is intrinsic: It depends only on the local geometry of the traveling wave front. We expect that one could

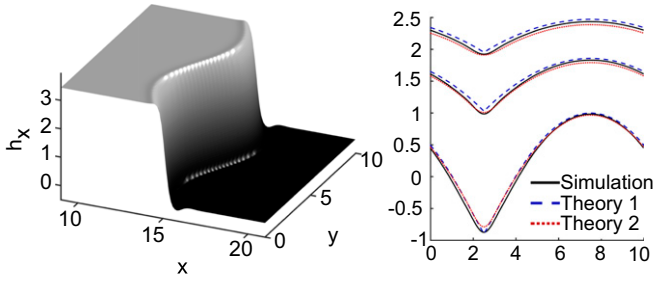

Fig. 2. Numerical tests comparing the curve evolution Eqs. **2** and **6** to simulations of the full dynamics (Eq. **1**). (*Left*) Initial surface slope $h_x(x,y,0) = s\left(x + \sin\left(\frac{2\pi}{10}y\right)\right)$. (*Right*) Curve extracted from full simulation (solid line), curve predicted by Eq. **2** (blue dashed line), and curve predicted by Eq. **6** (red dotted line), at times 2, 7.5, and 12 (corresponding to area doses 7.5, 28.125, and 45 nC/μm^2). The curves at each different time have been plotted at 1/10 the actual separation in the vertical direction.

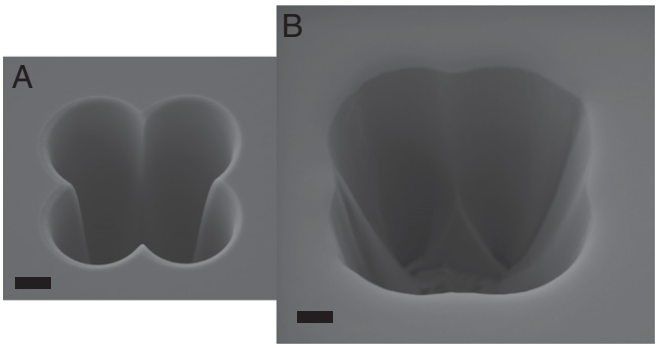

Fig. 3. (*A*) Initial milled "clover" pit and (*B*) milled pit after an area dose 30 nC/μm^2 imaged under SEM at 30° off-normal. (Scale bars, 2 μm and identical.)

derive Theory 1 from the governing Eq. **1** by considering a slowly varying traveling wave, and additionally that one could derive the next-order corrections to Eq. **2** as we have done in Theory 2. We do not do this here because, as we will show, the difference between the predictions of the two theories is so small as to be undetectable experimentally, but this would be an interesting question for future analysis.

Comparing Theories, Simulations, and Experiments. To test how well Eqs. **2** and **6** describe the propagation of steep features, we compared them with numerical simulations of the full 2D equations (Eq. **1**). We started with a traveling wave computed as a steady solution to the discretized version of Eq. **1**, applied a sinusoidal perturbation to the surface slope in the transverse direction, evolved this surface numerically, and identified the curve by the maximum of $|h_{xx}|$ as a function of y at each timestep. We compared this curve to numerical simulations of Eqs. **2** and **6** with the same sinusoidal initial condition (*Materials and Methods*).

Fig. 2 shows the three curves at different times. The curves predicted by the theories agree extremely well with the curve extracted from the simulations. This agreement is destroyed when the parameters are changed from their predicted values, so it is not an accident. The small discrepancies between theoretical predictions and simulations are thought to come from two sources: numerical discretization of the 2D equations and higher-order asymptotic corrections to the theoretical curves. It is notable that the curves predicted by both theories are also extremely close to each other, showing that although they make different kinds of approximations they may be used roughly interchangeably. Therefore, Theory 1 should be preferred under the conditions investigated here, because it is simpler.

We then compared experimental pit propagation to the predictions of Theories 1 and 2. We started with a clover-shaped hole, formed by milling four overlapping circular pits (Fig. 3) with radius 2.9 μm, centered at (±2.4 μm, ±2.4 μm). A fifth pit with radius 1.5 μm was milled at the origin to remove the extra material not removed by the other four pits. All pits were milled in parallel to minimize the effects of Si redistribution on pit walls. The initial and final pit morphologies, imaged using SEM at 30° off-normal, are shown in Fig. 3. The horizontal pit width expands from 10.8 μm to 15.7 μm after an area dose of 30 nC/μm^2 Ga^+.

We simulated the evolution of a curve using Eqs. **2** and **6** with initial condition set to the boundary of the clover-shaped hole. We fit the propagation speed c to that observed experimentally, because we were unable to match it quantitatively from first principles (*Supporting Information*, *Speed Calculations*). The simulated curves are overlaid on the real-time FIB images for comparison and shown after an area dose of 0.07 nC/μm^2, 15.00 nC/μm^2, and 30.00 nC/μm^2 in Fig. 4. Both simulations agree equally well with experiment, overlapping at the pit walls with greatest radius of curvature. At the four "kinks" with tighter radius of curvature, the simulated curves vary from experiment by an average of 0.1 μm. Both models could be used essentially indistinguishably in these experimental systems.

Solving the Inverse Problem. Our numerical simulations and experimental tests show that either Eq. **2** or Eq. **6** can be used to predict the propagation of steep regions on the surface. These are intuitive equations that make it easy to sketch by hand an approximate initial condition for a surface that evolves under bombardment to a given final pattern. In addition, because evolving a collection of curves is fast, the inverse problem can be efficiently solved more precisely by numerical methods, for example by Monte-Carlo simulations. To illustrate, we explain how we designed the lattice in Fig. 1*A*. Our target pattern is a periodic array of tiles shown in Fig. 5*A*. The black pixels are regions where we wish the surface to be elevated, where the borders are intended to be the knife-edge ridges. We will make this pattern using a periodic array of curves, each of the polar form $r(\theta) = r_0(1 + Re\{\sum_{k=-k_{max}}^{k_{max}} w_k e^{ik\theta}\})$, where $\{w_k\}_{k=-k_{max}}^{k_{max}}$ are parameters to be determined. We set $k_{max} = 8$ and require the pattern to be formed at a fixed simulation time T. These restrictions do not come from realistic experimental constraints, but rather are intended to illustrate the more general principle that one can optimize over a constrained set of initial conditions.

We then used Monte-Carlo simulations to find the initial conditions that lead to the desired pattern. At each Monte-Carlo step we varied one parameter, solved Eq. **6** up to time T, and computed the cost as the sum of the absolute discrepancy between the set of pixels lying outside each closed curve and the target pattern. We discarded moves that increased the cost with a cost-dependent probability. Fig. 5*B* shows the optimal initial condition after a large number of Monte-Carlo steps (blue) and the final curve that it evolves to (red). Fig. 1 *A*–*C* shows the evolution of this initial condition with a simulation of Eq. **1**; again there is excellent agreement.

Conclusion

We have introduced a method to make steep, sharp patterns on surfaces by prepatterning the surface so it dynamically evolves under uniform bombardment to something that is much smaller in scale and more difficult to make directly. Our method is based on the demonstration that for certain materials, ions, and energies the steep parts of the surface evolve as one-dimensional curves that propagate at a constant speed in the normal direction. This simplification agrees extremely well with simulations of the full nonlinear dynamics, and over large enough scales it also agrees with experimental measurements of the evolution of steep-walled pits under rastered FIB irradiation. On small scales, such as when steep features approach each other to form sharp ridges, the theory is not expected to apply because the governing equations are based on a small-curvature approximation, and indeed on these scales we observed several phenomena

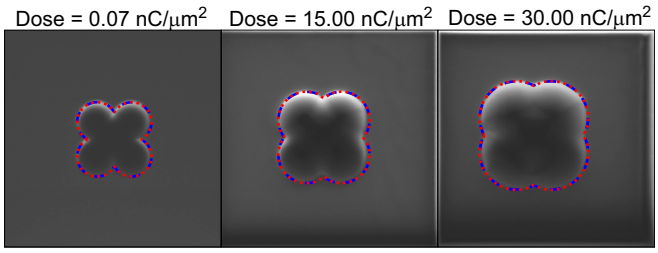

Fig. 4. The evolution of the clover-shaped pit under homogeneous FIB rastering of the entire imaged area, for irradiation doses indicated. Theoretical predictions using Eqs. **2** (blue) and **6** (red) are superimposed.

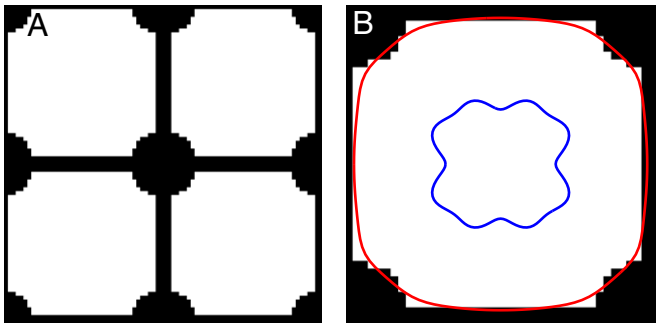

Fig. 5. (*A*) Target pattern used to design the lattice in Fig. 1, where black pixels are elevated regions. (*B*) Initial condition with lowest cost (blue) and curve it evolves to (red). The cost of this initial condition is the sum of the number of white pixels lying outside the red curve, plus the number of black pixels lying inside it.

that we do not yet understand. In addition, we were unable to quantitatively predict the speed of the curve from first principles, but it is easy to measure and then incorporate into the theory. Therefore, we propose that this method of evolving one-dimensional curves may be used as a first approximation to determining a surface's final structure after uniform bombardment.

Evolving curves is fast, so it naturally leads to efficient methods to solve the inverse problem of determining how to pattern the surface initially so it evolves to a desired target structure. We showed how to make a simple lattice connecting diamonds with steep ridges, but one can imagine making more complex patterns, for example by starting with several different shapes, nonclosed curves, bumps instead of pits, or undulating topography, and also by allowing the curves to continue evolving once they intersect, to form gaps. The space of possibilities is large and we expect that further understanding of the nonlinear dynamics of ion-bombarded surfaces will lead to new methods to invent and fabricate materials.

Materials and Methods

Experimental Methods. Samples were polished (001) Si wafers from Virginia Semiconductor, Inc. and were irradiated using a ZEISS NVision 40 FIB using NanoPatterning and Visualization Engine (NPVE) software. Samples were affixed to aluminum sample stubs using silver paste, and dust was removed using an air jet before loading into the FIB. The SEM beam was switched off during FIB irradiation to avoid the surface carbon contamination typical of SEM imaging. The ion beam was 30 keV Ga^+, with a current of 1.5 nA, beam diameter 200 nm, center-to-center dot spacing 100 nm, and dwell time 1.0 μs. Steep-walled pits were milled by rastering the beam repeatedly, each time delivering a small dose to the pit area and sputtering away a thin layer of Si. The beam was rastered over the milling area at least 10,000 times to create each pit, ensuring that the effects of nonuniform Si redistribution were minimized. Circular pits were created by rastering the beam in circles from the center outward to the outer rim to create a maximally clean, steep pit wall. Circular pits were overlapped to form the "clover" shapes. To cause pit evolution, a square bombardment area was chosen to overlap the pits. The same 1.5-nA, 30-keV FIB beam was then repeatedly rastered over this area in a double serpentine (boustrophedonic followed by its time-reverse) scan, delivering a small dose in each pass to approximate uniform irradiation. A depth of ∼0.5 nm of material was sputtered away with each pass of the beam. Images of the pit shape were captured during irradiation using FIB imaging using the secondary electron (SE2) detector. Initial and final morphology were imaged using SEM.

We found that the pit wall propagation rate was slower than the theoretically predicted rate; to counteract this discrepancy and ensure impingement occurred at the correct moment during pit evolution, the initial pits were milled closer than directed by the simulations.

Numerical Methods. All numerical simulations were performed using an erosion function for 30 keV Ga^+ on Si, found in ref. 20 to be

$$R(b) = R(0)\frac{\sqrt{1+b^2}}{\sqrt{1+b^2\mu^2/\sigma^2}} \times \exp\left\{-\frac{a^2/\sigma^2}{2(1+b^2\mu^2/\sigma^2)}+\frac{a^2/\sigma^2}{2}-\Sigma\left(\sqrt{1+b^2}-1\right)\right\}, \quad [7]$$

with parameters $a/\sigma = 2.04$, $\mu/\sigma = 0.658$, and $\Sigma = 0.0462$.

To simulate Eq. **1**, we nondimensionalized the equation by scaling lengths by $L = (B_0/R_0)^{1/3}$, times by $T = L/R_0$, and the yield function by $R(b) \to R(b)/R_0$, where $R_0 = R(0)$. We then used a nondimensional parameter $\bar{B}_0 = 0.02$ so we could simulate scales much large than the width of the traveling wave. We used a semiimplicit numerical method introduced in ref. 24. The discretization changes the undercompressive slope and speed from their theoretical nondimensional values of $b_0 = 3.89$, $c = 1.73$ to $b_0 = 3.45$, $c = 1.84$. We used the numerical values in Eqs. **2** and **6** when comparing to simulations.

We simulated Eq. **6** using the same semiimplicit method as ref. 24 but applied to a one-dimensional equation. For radial pits we assumed the phase ψ was a perturbation to the radius $r(t)$ so changed to radial coordinates by making the substitution $\partial_y \to r^{-1}\partial_y$. Coefficients c_i were calculated numerically by first computing the undercompressive traveling wave solution $s(\eta)$ using MATLAB's bvp solver then computing $a_i(s)$ using centered differences for the derivatives, and finally computing $\pi(\eta)$ as the second element in the null space of the numerically discretized version of $\mathcal{L}$ in Eq. **5** (the first element of the discretized operator is always constant.) We performed an affine transformation on π to ensure it had the correct boundary conditions because these are not required for the discretized operator. The traveling wave and coefficients were calculated for the nondimensional equation and were redimensionalized using $B_0 = 0.02$ to compare with simulations and experiments. The nondimensional values were $c_2 = 0.866$, $c_3 = -0.245$, and $c_4 = 0.231$. To redimensionalize we multiply c_2 by $L/T = R_0$, c_3 by $L^2/T = R_0^{2/3}B_0^{1/3}$, and c_4 by $L^4/T = B_0$ (note that ψ has units of length). For the experiments, we do not know the true value of B_0, but as long as it is small it makes little difference to the curve dynamics.

We simulated Eq. **2** by discretizing the curve, calculating tangent vectors with centered differences, and updating each point on the curve according to Eq. **2**. To prevent the curve from self-intersecting we added a small term $\epsilon\kappa_1$ to the right-hand side, where κ_1 is the curvature vector, calculated using centered differences on the normalized tangent vectors. When the minimum separation between the points parameterizing the curve dropped below a threshhold we reparameterized, by linear interpolation. This step provides a smoothing that in some cases was sufficient to prevent the curve from self-intersecting, so we could use $\epsilon = 0$. Otherwise, we chose $\epsilon = 1 \times 10^{-5}$. This value was small enough that the evolution was indistinguishable by eye from a curve that evolves with $\epsilon = 0$ over the regions that have not yet self-intersected.

ACKNOWLEDGMENTS. This research was funded by the National Science Foundation (NSF) through Harvard Materials Research Science and Engineering Center Grant DMR-1420570 and Division of Mathematical Sciences Grant DMS-1411694. This work was also supported by NSF Grant DMR-1409700 (to J.C.P. and M.J.A.). This work was performed in part at the Center for Nanoscale Systems (CNS), a member of the National Nanotechnology Infrastructure Network, which is supported by NSF Grant ECS-0335765. CNS is part of Harvard University. M.P.B. is an Investigator of the Simons Foundation.

1. Vasile MJ, Niu Z, Nassar R, Zhang W, Liu S (1997) Focused ion beam milling: Depth control for three-dimensional microfabrication. *J Vac Sci Technol B* 15(6):2350–2354.
2. Adams D, Vasile M, Mayer T, Hodges V (2003) Focused ion beam milling of diamond: Effects of H_2O on yield, surface morphology and microstructure. *J Vac Sci Technol B* 21(6):2334–2343.
3. Li J, et al. (2001) Ion-beam sculpting at nanometre length scales. *Nature* 412(6843): 166–169.
4. Stein D, Li J, Golovchenko JA (2002) Ion-beam sculpting time scales. *Phys Rev Lett* 89(27):276106.
5. Sigmund P (1969) Theory of sputtering. I. Sputtering yield of amorphous and polycrystalline targets. *Phys Rev* 184(2):383–416.
6. Sigmund P (1973) A mechanism of surface micro-roughening by ion bombardment. *J Mater Sci* 8(11):1545–1553.
7. Bradley RM, Harper JME (1988) Theory of ripple topography induced by ion bombardment. *J Vac Sci Technol A* 6(4):2390–2395.
8. Chan WL, Chason E (2007) Making waves: Kinetic processes controlling surface evolution during low energy ion sputtering. *J Appl Phys* 101(12):121301.
9. Muñoz-Garcia J, et al. (2009) Self-organized surface nanopattering by ion beam sputtering. *Toward Functional Nanomaterials*, Lecture Notes in Nanoscale Science and Technology (Springer, New York), pp 323–398.
10. Facsko S, et al. (1999) Formation of ordered nanoscale semiconductor dots by ion sputtering. *Science* 285(5433):1551–1553.

11. Frost F, Schindler A, Bigl F (2000) Roughness evolution of ion sputtered rotating InP surfaces: Pattern formation and scaling laws. *Phys Rev Lett* 85(19):4116–4119.
12. Cuenat A, George HB, Chang KC, Blakely J, Aziz MJ (2005) Lateral templating for guided self-organization of sputter morphologies. *Adv Mater* 17(23):2845–2849.
13. Castro M, Cuerno R, Vázquez L, Gago R (2005) Self-organized ordering of nanostructures produced by ion-beam sputtering. *Phys Rev Lett* 94(1):016102.
14. Wei Q, et al. (2008) Ordered nanocrystals on argon ion sputtered polymer film. *Chem Phys Lett* 452(1):124–128.
15. Ziberi B, Front F, Tartz M, Neumann H, Rauschenbach B (2008) Ripple rotation, pattern transitions, and long range ordered dots on silicon by ion beam erosion. *Appl Phys Lett* 92(6):063102.
16. Muñoz-García J, Gago R, Vázquez L, Sánchez-García JA, Cuerno R (2010) Observation and modeling of interrupted pattern coarsening: Surface nanostructuring by ion erosion. *Phys Rev Lett* 104(2):026101.
17. Bradley RM, Shipman PD (2010) Spontaneous pattern formation induced by ion bombardment of binary compounds. *Phys Rev Lett* 105(14):145501.
18. Smythe EJ, Cubukcu E, Capasso F (2007) Optical properties of surface plasmon resonances of coupled metallic nanorods. *Opt Express* 15(12):7439–7447.
19. Rockstuhl C, et al. (2006) On the reinterpretation of resonances in split-ring-resonators at normal incidence. *Opt Express* 14(19):8827–8836.
20. Chen HH, et al. (2005) Shocks in ion sputtering sharpen steep surface features. *Science* 310(5746):294–297.
21. Miller MK, Russell KF, Thompson GB (2005) Strategies for fabricating atom probe specimens with a dual beam FIB. *Ultramicroscopy* 102(4):287–298.
22. Loi ST, Gault B, Ringer SP, Larson DJ, Geiser BP (2013) Electrostatic simulations of a local electrode atom probe: The dependence of tomographic reconstruction parameters on specimen and microscope geometry. *Ultramicroscopy* 132:107–113.
23. Holmes-Cerfon M, Aziz M, Brenner MP (2012) Creating sharp features by colliding shock on uniformly irradiated surfaces. *Phys Rev B* 85(16):165441.
24. Holmes-Cerfon M, Zhou W, Bertozzi AL, Brenner MP, Aziz MJ (2012) Development of knife-edge ridges on ion-bombarded surfaces. *Appl Phys Lett* 101(14):143109.
25. Osher S, Sethian J (1988) Fronts propagating with curvature-dependent speed: algorithms based on Hamilton-Jacobi formulations. *J Comput Phys* 79(1):12–49.
26. Sethian J (1996) *Level Set Methods: Evolving Interfaces in Geometry, Fluid Mechanics, Computer Vision and Material Sciences* (Cambridge Univ Press, Cambridge, UK).
27. Madi CS, Anzenberg E, Ludwig KF, Jr, Aziz MJ (2011) Mass redistribution causes the structural richness of ion-irradiated surfaces. *Phys Rev Lett* 106(6):066101.
28. Norris SA, et al. (2011) Molecular dynamics of single-particle impacts predicts phase diagrams for large scale pattern formation. *Nat Commun* 2:276.
29. Aziz MJ (2006) Nanoscale morphology control using ion beams. *Matematisk-Fysiske Meddelelser* (Royal Danish Academy of Sciences and Letters, Copenhagen), Vol 52, pp 187–206.
30. Mullins W (1959) Flattening of a nearly plane solid surface due to capillarity. *J Appl Phys* 30(1):77.
31. Herring C (1950) Effect of change of scale on sintering phenomena. *J Appl Phys* 21(4): 301.
32. Umbach CC, Headrick RL, Chang KC (2001) Spontaneous nanoscale corrugation of ion-eroded SiO2: The role of ion-irradiation-enhanced viscous flow.$_2$ *Phys Rev Lett* 87(24): 246104.
33. Davidovitch B, Aziz MJ, Brenner MP (2009) Linear dynamics of ion sputtered surfaces: Instability, stability and bifurcations. *J Phys Condens Matter* 21(22):224019.
34. Bertozzi A, Munch A, Shearer M (1999) Undercompressive shocks in thin film flows. *Physica D* 134(4):431–464.
35. Bertozzi A, Munch A, Shearer M, Zumbrun K (2001) Stability of compressive and undercompressive thin film travelling waves. *Eur J Appl Math* 12(3):253–291.
36. LeFloch PG, Mohammadian M (2008) Why many theories of shock waves are necessary: Kinetic functions, equivalent equatinos, and fourth-order models. *J Comput Phys* 227(8):4162–4189.
37. Bender C, Orszag S (1999) *Advanced Mathematical Methods for Scientists and Engineers: Asymptotic Methods and Perturbation Theory* (Springer, Berlin).
38. Liu TP, Zumbrun K (1995) On nonlinear stability of general undercompressive viscous shock waves. *Commun Math Phys* 174(2):319–345.
39. Sattinger DH (1976) On the stability of waves of nonlinear parabolic systems. *Adv Math* 22(3):312–355.
40. Zumbrun K, Serre D (1999) Viscous and inviscid stability of multi-dimensional planar shock fronts. *Indiana Math J* 48(3):937–992.
41. Giannuzzi L, Stevie F, eds (2005) *Introduction to Focused Ion Beams: Instrumentation, Theory, Techniques and Practice* (Springer, Berlin), pp 329–331.
42. Yamamura Y, Itikawa Y, Itoh N (1983) Angular dependence of sputtering yields of monatomic solids. Report No. IPPJ-AM-26 (Institute of Plasma Physics, Nagoya University, Nagoya, Japan).
43. Yamamura Y, Mössner C, Oechsner H (1987) The bombarding-angle dependence of sputtering yields under various surface conditions. *Radiat Eff* 103(5):25–43.
44. Shraiman BI (1986) Order, disorder, and phase turbulence. *Phys Rev Lett* 57(3): 325–328.
45. Bernoff AJ (1988) Slowly varying fully nonlinear wavetrains in the ginzburg-landau equation. *Physica D* 30(3):363–381.

Supporting Information

Perkinson et al. 10.1073/pnas.1609315113

Speed Calculations

According to the theory, the speed c of the curves is uniquely determined by the yield curve and the type of smoothing physics (but not its magnitude). We compared theory to experiments, starting from the previously measured yield curve and our best knowledge of the smoothing physics, believed to be surface diffusion.

In Fig. 4, shocks were measured moving 80 nm over a delivered area dose of 1 nC/μm^2. For the flux used in that experiment, this area dose corresponds to a time of 602 s. Thus, the experimental shock propagation speed is found to be 80 nm/602 s = 0.13 nm/s.

The shock speed is theoretically given as $c=(R(b_0)-R(0))/(b_0-0)$ and depends on the fixed slope b_0 and the erosion velocities $R(b_0)$ and $R(0)$. The slope is $b_0=3.89$ as described by Chen et al. (20). Theoretical values for the erosion velocities $R(b)$ can be derived using the sputter yield $Y(b)$, a measure of atoms sputtered away from the surface per incident ion, by changing dimensions. The sputter yield for normal incidence ions, $Y(0)=2.78$, is found using SRIM simulations and reported by Giannuzzi and Stevie (41), which along with the equation for the angular dependence of the normalized sputter yield modified by the empirical Yamamura correction factor (42, 43) yields a value of $Y(b_0)=21.5$. The dimensional erosion velocities can be calculated using these sputter yields and the atomic volume of silicon, 2.00×10^{-29} m^3:

$$R(0)=\frac{1\ \text{nC}/\mu\text{m}^2}{602\ \text{s}}\left(\frac{6.24\times10^9\ \text{ions in}}{1\ \text{nC}}\right)\left(\frac{2.78\ \text{atoms out}}{\text{ions in}}\right)\times\left(\frac{2.00\times10^{-29}\ \text{m}^3}{\text{atoms out}}\right)\left(\frac{10^{18}\mu\text{m}^3}{1\ \text{m}^3}\right)\left(\frac{10^3\ \text{nm}}{1\ \mu\text{m}}\right)=0.576\ \text{nm/s}$$

$$R(b_0=3.89)=\frac{1\ \text{nC}/\mu\text{m}^2}{602\ \text{s}}\left(\frac{6.24\times10^9\ \text{ions in}}{1\ \text{nC}}\right)\left(\frac{21.5\ \text{atoms out}}{\text{ions in}}\right)\times\left(\frac{2.00\times10^{-29}\ \text{m}^3}{\text{atoms out}}\right)\left(\frac{10^{18}\ \mu\text{m}^3}{1\ \text{m}^3}\right)\left(\frac{10^3\ \text{nm}}{1\ \mu\text{m}}\right)=4.456\ \text{nm/s}.$$

The shock speed from theory is thus $c=(4.456\ \text{nm/s}-0.576\ \text{nm/s})/(3.89-0)=0.997$ nm/s, a factor of 8 larger than that measured from experiment.

This discrepancy means that either there is something wrong with the yield curve or there is smoothing physics that is not yet incorporated in the model. We do not understand this discrepancy and leave it as a question for future research. Note, however, that this discrepancy is not important for the theory in this paper, because the theory only requires that the speed and slope be uniquely selected. We can simply measure the shock front velocity by evolving circular pits and use this measured velocity to evolve shapes.

Knife-Edge Ridge Curving After Initial Formation

Simulation and experiment both demonstrate that knife-edge ridges become curved if irradiation continues after the initial impingement of steep features, as shown in Fig. S1. The shape of the wall, with a central high point, arises due to the slight curvature remaining in the shape of the propagating walls at the moment of impingement, which causes the midpoint of the ridge to form later than the rest of the ridge. This central high point is absent from the ridges shown in Fig. 1*E* because initial pits were spaced further apart, resulting in a more uniformly round shape at the moment of bombardment. Furthermore, because the pits "reached out" to each other when they evolved within 200 nm of each other, the center of the ridge formed first, thus removing the source of the central high point.

Detailed Multiscale Calculations

In this section we record the details of the multiscale expansion used to derive Eq. **6**, the basis of Theory 2. We work in the frame of reference of the traveling wave by defining $\eta=x-ct$. The η-derivative of Eq. **1** is

$$(h_\eta)_t+(R(b))_\eta-ch_{\eta\eta}+B_0\partial_\eta\nabla\cdot(f(b)\nabla\nabla\cdot(f(b)\nabla h)), \qquad \textbf{[S1]}$$

with $f(b)=(1+b^2)^{-1/2}$, $b=|\nabla h|=\sqrt{h_x^2+h_y^2}$. We make the ansatz $h=S(x-ct+\Psi(y,t))+h_0(t)+\epsilon h_1+\epsilon^2h_2+\ldots$, where $s(\eta)=S'(\eta)$ is the traveling wave solution, and assume the scalings $\partial_t\sim O(\epsilon)$, $\partial_y\sim O(\epsilon^{1/2})$.

The $O(1)$ and $O(\epsilon)$ parts of various terms are shown in the table below. The fourth-order term has been broken up by first calculating $k(b)=\nabla\cdot(f(b)\nabla h)=\partial_\eta(fh_\eta)+\partial_y(fh_y)$ and then calculating $m(b)=\partial_\eta\nabla\cdot(f(b)\nabla k(b))$.

To distinguish between various derivatives, we write a subscript "d" when we mean the pointwise derivative of a function,with no chain rule involved, that is, $f_d(s(\eta))=\frac{d}{ds}f|_{s(\eta)}$. We write a prime symbol to mean derivative with respect to η, that is, $f'(s)=f_d(s)s'(\eta)$. All functions are evaluated at s.

	$O(1)$	$O(\epsilon^{1/2})$	$O(\epsilon)$
h	$S+h_0(t)$		h_1
h_t	$s+\frac{d}{dt}h_0$		$s\psi_t+h_{1,t}$
h_η	s		$h_{1,\eta}$
$h_{\eta\eta}$	s'		$h_{1,\eta\eta}$
h_y		$s\psi_y$	
h_{yy}			$\psi_y^2s'+s\psi_{yy}$
b	s		$\frac{1}{2}s\psi_y^2+h_{1,\eta}$
$f(b)$	$f(s)$		$f_d\left(\frac{1}{2}s\psi_y^2+h_{1,\eta}\right)$
f_y		$f'\psi_y$	
$(R(b))_\eta$	$(R(s))'$		$\left(\frac{1}{2}R_ds\right)'\psi_y^2+(R_d(s))'h_{1,\eta}+R_dh_{1,\eta\eta}$
$k(b)$	$(fs)'$		$\partial_\eta[(f_ds+f)h_{1,\eta}]+fs\psi_{yy}+\left(\frac{1}{2}f_ds^2+fs\right)'\psi_y^2$
κ_y		$(fs)''\psi_y$	
$m(b)$	$(f(fs)'')''$		$=\partial_{\eta\eta}(f_0k_{1,\eta}+f_1k_{0,\eta})+\partial_\eta\partial_y(f_0k_{0,y})$
			$=\psi_{yy}\cdot((f(fs)'')'+(fs)''')$
			$+\psi_y^2\cdot\left(\left(\frac{1}{2}f_ds(fs)''\right)''+(f(fs)'')''\right.$
			$\left.+(f(fs')')''+\left(f\left(\frac{1}{2}f_ds^2\right)''\right)''\right)$
			$+(f((f_ds+f)h_{1,\eta})'')''+(f_d(fs)''h_{1,\eta})''$

Some auxiliary calculations are given below:

$f_0k_{1,\eta}$	$=f\partial_{\eta\eta}[(f_ds+f)h_{1,\eta}]+f(fs)'\psi_{yy}+f\left(\frac{1}{2}f_ds^2+fs\right)''\psi_y^2$
$f_1k_{0,\eta}$	$=\frac{1}{2}f_ds(fs)''\psi_y^2+f_d(fs)''h_{1,\eta}$
$\partial_y(f_0k_{0,y})$	$=(f(fs)'')'\psi_y^2+f(fs)''\psi_{yy}$

Collecting up terms gives the $O(1)$ equation

$$\partial_{\eta\eta}\left(f(s)\partial_{\eta\eta}(f(s)s)\right)+(R(s))'-cs'=0. \qquad \textbf{[S2]}$$

This equation is satisfied by construction, because $s(\eta)$ is assumed to be a solution.

Next we collect up terms for the $O(\epsilon)$ equation, and also include the term for ψ_{yyyy} from the $O(\epsilon^2)$ equation. We obtain, with $u = h_{1,\eta}$:

$$u_t + \mathcal{L}u = a_1(s)\psi_t + a_2(s)\psi_y^2 + a_3(s)\psi_{yy} + a_4(s)\psi_{yyyy}. \quad \text{[S3]}$$

The linear operator is

$$\mathcal{L}u = ((R_d - c)u)' + B_0\left[\left(f_d(fs)''u\right)'' + \left(f((f_d s + f)u)''\right)''\right], \quad \text{[S4]}$$

and the coefficients are

$$a_1(s) = s' \quad \text{[S5]}$$

$$a_2(s) = \frac{1}{2}(R_d s)' + B_0\left[\frac{1}{2}(f_d s(fs)'')'' + (f(fs)'')'' + \left(f\left(\frac{1}{2}f_d s^2 + fs\right)''\right)''\right] \quad \text{[S6]}$$

$$a_3(s) = B_0\left[(f(fs)'')' + (f(fs)')''\right] \quad \text{[S7]}$$

$$a_4(s) = B_0(f^2 s)'. \quad \text{[S8]}$$

Boundary Conditions for the Undercompressive Wave

We elaborate on the boundary conditions used in the solvability condition in the paragraph following Eq. **6**. These were justified rigorously in ref. 35, but we include a heuristic version of the argument here for completeness, treating all possible types of traveling wave solutions to Eq. **1**.

A general one-dimensional traveling wave solution has the form $h_x = s(x - ct)$ and solves

$$c(s - b_r) - (R(s) - R(b_r)) - B_0\left(\frac{1}{\sqrt{1+s^2}}\left(\frac{s'}{(1+s^2)^{3/2}}\right)'\right)' = 0, \quad \text{[S9]}$$

with boundary conditions $s(-\infty) = b_l$, $s(+\infty) = b_r$, where b_l, b_r are parameters (23). The wave speed is found by integrating from $-\infty$ to $+\infty$ to be $c = (R(b_r) - R(b_l))/(b_r - b_l)$. There are three types of waves, characterized by the relation between c and the speed $R'(b_{l(r)})$ of information propagation on either side of the wave:

- A compressive wave has $R'(b_l) > c > R'(b_r)$, so that information propagates into the wave from both sides.
- An undercompressive wave has $R'(b_l) \langle c \rangle R'(b_r)$ or $R'(b_l) > c < R'(b_r)$, so that information propagates in on one side and away on the other.
- A doubly undercompressive wave has $R'(b_l) < c < R'(b_r)$, so that information propagates away on both sides.

A useful way of identifying the type of wave is by the dimensions of the invariant manifolds at the endpoints (23, 34). Because Eq. **S9** is third-order, a traveling wave can be thought of as a trajectory (s, s', s'') in $\mathbb{R}^3$ connecting point $(b_l, 0, 0)$ to point $(b_r, 0, 0)$. It must lie in the intersection of the unstable manifold at $\eta = -\infty$ [written $\mathcal{US}(-\infty)$] and the stable manifold at $\eta = +\infty$ [written $\mathcal{S}(\infty)$]. Linearizing Eq. **S9** and looking for exponentially growing modes $\propto e^{\mu\eta}$ shows that $\mu^3 \propto c - R'(b_{l(r)})$, so $\mathcal{US}(-\infty)$ is 2D when $c < R'(b_l)$ and one-dimensional otherwise, and $\mathcal{S}(\infty)$ is 2D when $c > R'(b_r)$ and one-dimensional otherwise. Therefore, a compressive wave occurs when the two invariant manifolds are 2D, an undercompressive wave when one is one-dimensional and the other is 2D, and a doubly undercompressive wave when both are one-dimensional.

To determine the boundary conditions for the equation $\mathcal{L}^*\pi = 0$, we analyze the left and right eigenfunctions of the linear operator $\mathcal{L}$. We have that $\mathcal{L}s' = 0$, because this is simply the linearization of Eq. **S9**. Therefore, 0 is an eigenvalue of $\mathcal{L}$ with right eigenfunction s', so there is a corresponding left eigenfunction π such that $\langle \pi, s' \rangle = 1$. To find the boundary conditions that make this normalization possible, we perturb the operator as $\mathcal{L}_\delta = \mathcal{L} + \delta\mathcal{L}_1$ and suppose it is analytic at the origin, so that the eigenvalues and eigenfunctions also have a perturbation expansion as*

$$\phi_\delta = \phi + \delta\phi_1 + \delta^2\phi_3 + \cdots, \quad \pi_\delta = \pi + \delta\pi_1 + \delta^2\pi_2 + \cdots, \quad \lambda_\delta = 0 + \delta\lambda_1 + \delta^2\lambda_2 + \cdots \quad \text{[S10]}$$

Here ϕ_δ is the right eigenfunction of $\mathcal{L}_\delta$, π_δ is the left eigenfunction, and λ_δ is the eigenvalue. $\mathcal{L}^*$ will have the same leading-order boundary conditions as $\mathcal{L}_\delta^*$, which follow by considering the growth of ϕ_δ, π_δ near $\pm\infty$ and the condition $\langle \phi_\delta, \pi_\delta \rangle < \infty$. Consider each case in turn:

- Compressive: Then $\mathcal{US}(-\infty)$, $\mathcal{S}(\infty)$ are both 2D, so generically they still intersect in a trajectory when perturbed. Therefore, ϕ_δ decays exponentially on both sides, so π_δ can grow on both sides. Requiring it to be bounded implies $|\pi(-\infty)|, |\pi(\infty)| < const.$

In this case the solution to $\mathcal{L}^*\pi = 0$ is $\pi = const$; this solution is what one typically expects, for example for periodic traveling waves (e.g., refs. 44 and 45). The constants in Eq. **6** are computed analytically as

$$\bar{c}_1 = (b_r - b_l), \quad \bar{c}_2 = R_d(b_r)b_r - R_d(b_l)b_l, \quad \bar{c}_3 = 0, \quad \bar{c}_4 = f^2(b_r)b_r - f^2(b_l)b_l, \quad \text{[S11]}$$

where $\bar{c}_i = \langle \pi, a_i(s) \rangle$.

- Undercompressive: If one of the invariant manifolds is one-dimensional, then generically a perturbation to the equation will destroy the intersection. If $\mathcal{US}(-\infty)$ is one-dimensional, then ϕ_δ will grow exponentially on the left, so π_δ must decay exponentially on the left to satisfy $\langle \phi, \pi \rangle < \infty$. Requiring it to be bounded implies the boundary conditions $\pi(-\infty) = 0$, $\pi(\infty) = const$; the constant can be chosen without loss of generality to be 1.
- Doubly undercompressive: A similar discussion to the undercompressive case implies the boundary conditions are $\pi(-\infty) = 0$, $\pi(\infty) = 0$.

Which Terms to Include in Theory 2?

Here, we justify including a fourth-order term $c_4\psi_{yyyy}$ in Eq. **6**.

The multiscale expansion to $O(\epsilon)$ would include only the terms $c_2\psi_y^2$, $c_3\psi_{yy}$. We have found that the viscous term $c_3\psi_{yy}$ is sometimes very small—for a compressive wave $c_3 = 0$ (this is explained in *Supporting Information*, *Boundary Conditions for the Undercompressive Wave*), and for an undercompressive wave we have found that by varying $R(b)$ the magnitude of c_3 can sometimes be very small. In addition there is no guarantee that the sign is positive. With no viscous or fourth-order term, there is no smoothing mechanism: Eq. **6** is a Hamilton–Jacobi equation that advects ψ_y while causing it to sharpen until its derivatives blow up. Therefore, smaller length scales are created and terms from the second-order equation will become as important as those in the first-order equation in the regions of high gradient.

Which terms will be the first to become large? To answer this question, we proceed as in a boundary-layer analysis and seek the largest length scale $L(\epsilon)$ such that at least one higher-order term becomes $O(\epsilon)$ under the scaling $\bar{y} = (L(\epsilon))^{-1}y$. In introducing this

*Technically this operator as defined is not analytic at 0, but it can be made analytic by an appropriate change of variables; see ref. 35.

new scale we assume that ψ_y maintains its original magnitude, that is, $\psi_y \sim O(\epsilon^{1/2})$, but that its derivatives can become large due to the Hamilton–Jacobi dynamics. We look at the terms in the $O(\epsilon^2)$ equation, which has the form[†]

$$\begin{aligned} v_t + \mathcal{L}v = {} & (\cdot)\psi_{yyyy} + (\cdot)\psi_y\psi_{yyy} + (\cdot)\psi_{yy}^2 + (\cdot)\psi_y^2\psi_{yy} + (\cdot)\psi_y^4 \\ & + ((\cdot)u)_\eta\psi_y^2 + (\cdot)u_{\eta\eta\eta}\psi_{yy} + (\cdot)u_{\eta\eta\eta y}\psi_y + (\cdot)u_{\eta\eta\eta\eta}\psi_y^2 \\ & + u_\eta\psi_{\bar{\imath}} + \left((\cdot)\int_\eta u_y\right)_\eta\psi_y + \left((\cdot)u^2\right)_\eta + (\cdot)u_{\eta\eta yy}. \end{aligned} \quad \text{[S12]}$$

[†]Eq. S12 is the expansion using a linearized fourth-order term $\propto \Delta^2 h$; the expansion for the full nonlinear smoothing is similar but has more terms.

Here, v is the $O(\epsilon^2)$ perturbation to h_x, and $(\cdot)$ represents some function of $s(\eta)$. Somewhat surprisingly, the right-hand side includes terms proportional to $u_{(\cdot)}$. For a compressive wave, the coefficients of these terms after integrating over the fast variables are $c_i = 0$, but for a noncompressive wave the perturbations evolve nonlinearly in general (38).

By applying the new scaling to each of the terms, we find that when $L(\epsilon) = \epsilon^{1/6}$ then $\psi_{yyyy} \to \psi_{\bar{y}\bar{y}\bar{y}\bar{y}} \sim \epsilon^{1/2+3\cdot 1/6} = \epsilon$ but that all other terms are higher-order. Therefore, we include this term and obtain a well-posed curve evolution equation: Smaller scales can be created by the Hamilton–Jacobi dynamics, but these are subsequently suppressed by the fourth-order smoothing before other terms become important.

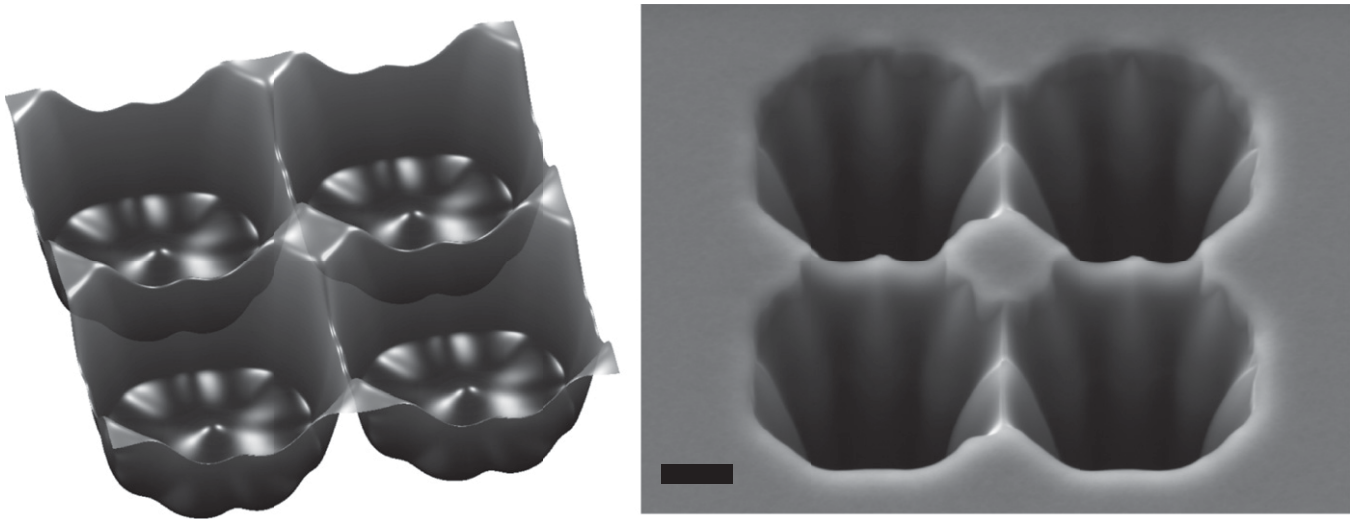

Fig. S1. (*Left*) Simulated knife-edge ridge behavior if irradiation continues after steep feature impingement. The initial hole had a nondimensional depth of −4, and the simulation was run until simulation time 1.8. (*Right*) SEM image of curved pit walls resulting from irradiation after steep feature impingement, viewed at 30° off-normal. Initial pits were milled with centers 3.4 μm apart and irradiated with an area dose of 1.2 nC/μm^2. (Scale bar, 2 μm.)

COMMENTARY

Designer shocks for carving out microscale surface morphologies

Andrea L. Bertozzi[a,1]

Shockwaves are propagating disturbances with a long history of study in gas dynamics, fluid dynamics, and astrophysics. We also see examples of shocks in everyday life such as a traffic jam, in which the oncoming traffic has much lower density than the cars within the traffic jam.

A classical compression wave involves propagation of a discontinuity in which information is absorbed from both sides in the shock layer. Undercompressive shocks are more unusual; they have special properties, including the transfer of information through the shock and often different stability properties than their compressive cousins. In the past decade, undercompressive waves have been studied in microscale and nanoscale applications in which surface forces dominate the physics in the shock layer. These forces can permit the existence of undercompressive waves, and their utility is just now coming to fruition. In PNAS, Perkinson et al. (1) demonstrate how to use undercompressive shocks in ion-bombarded surfaces to create patterns with steep ridges on a micrometer scale.

The traffic jam example is one that can be modeled with a simple 1D, first-order, nonlinear wave equation, or "conservation law," introduced in the mid-1950s (2, 3):

$$u_t + f(u)_x = 0. \quad [1]$$

Here, u is the material being transported in the direction x and f is the flux of the material. A shock is a solution to such an equation with a discontinuity in u that travels with speed s given by the Rankine–Hugoniot jump condition:

$$s = \frac{f(u_L) - f(u_R)}{u_L - u_R}.$$

Such models can be solved exactly for any choice of states u_L and u_R on the left and right of the discontinuity. All such shockwaves are compressive, meaning that they satisfy an entropy condition: The speed s of the shock is faster than the characteristics speed $f'(u_R)$ ahead of it and slower than the speed $f'(u_L)$ behind it. It was traditionally thought that any physical process described by such a simple 1D model could have only compressive shocks. This fact can be proved rigorously in the case where the physics in the shock layer is "diffusion" or Brownian motion, as is seen in gas dynamics. The modification of Eq. **1** to include linear diffusion in the shock layer is

$$u_t + f(u)_x = u_{xx}. \quad [2]$$

With diffusion, shock discontinuities are smoothed; however, the basic shock structure, including the speed of the shock as determined by the Rankine–Hugoniot jump condition, is exhibited in smooth traveling wave solutions of Eq. **2**. More recently, a number of "scalar law" physical systems have been identified that produce undercompressive shocks. The model considered by Perkinson et al. (1) involves an equation of motion for the slope of the surface of the form shown in Eq. **1** with additional physics in the shock layer from surface diffusion, resulting in a model similar to Eq. **2** with additional fourth-order diffusion on the right-hand side. A 1D nonlinear model for ion beam sputtering was introduced in 2005 by Chen et al. (4), who showed that it produced undercompressive shocks that could be reproduced in experiments. The model is a conservation law in which u is the slope of the surface and the nonlinear flux function f is the yield function, which gives the average velocity of erosion of the surface as a function of its local slope, and is, in general, nonconvex. Their model has a fourth-order term that models additional smoothing effects such as Mullins–Herring surface diffusion or ion-enhanced viscous flow confined to a thin surface layer. They showed that stable steep undercompressive waves were experimentally viable in ion-bombarded surfaces with common physical parameters.

In the case of compressive shocks, information travels into the shock from both sides. This idea is illustrated in Fig. 1*C*. In the case of an undercompressive shock, information enters the shock from one direction only (Fig. 1*D*). It will generally pass through the shock and exit the shock on the other side. Undercompressive

[a]Department of Mathematics, University of California, Los Angeles, CA 90095

Author contributions: A.L.B. wrote the paper.

The author declares no conflict of interest.

See companion article on page 11425.

[1]Email: bertozzi@math.ucla.edu.

www.pnas.org/cgi/doi/10.1073/pnas.1615158113

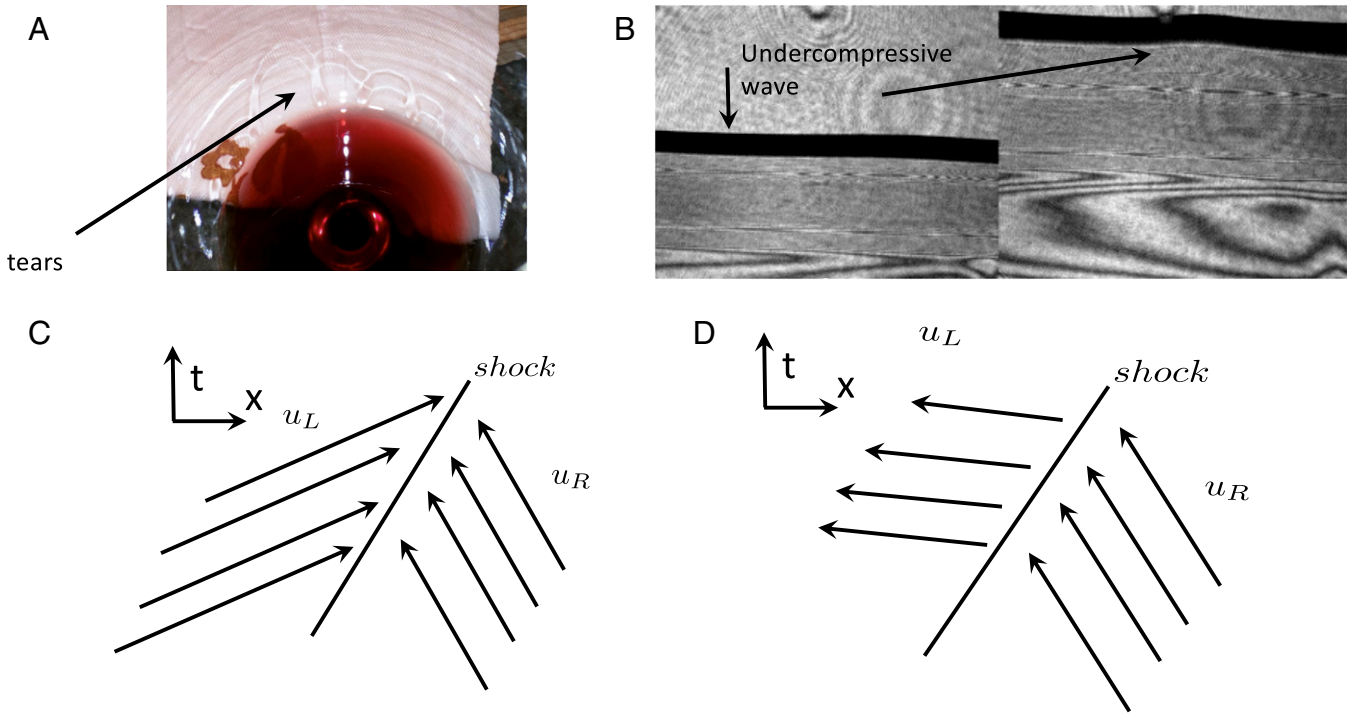

Fig. 1. (*A*) Tears of wine. (*B*) An undercompressive–compressive shock pair in a thermally driven coating flow showing two successive snapshots in time. The undercompressive shock is thick and dark, indicating a steep change in height using interferometry. Reproduced from ref. 14 with permission from Elsevier. (*C*) Characteristic diagram of a compressive shock. (*D*) Characteristic diagram of an undercompressive shock.

shocks can arise in 1D conservation laws when the correct physics in the shock layer is something other than second-order diffusion. Mathematical examples were first constructed for diffusive–dispersive equations, but without any direct comparison with physical experiments (5). About 10 y ago, a set of experiments involving driven thin films confirmed the presence of undercompressive shocks in the micrometer-scale coating flows driven by thermal gradients (6). For such systems, the dominant physics in the shock layer was not diffusion but, rather, surface tension on the air–liquid interface of the free surface of the film. Compressive shocks in driven films are well known; the most common example is the case of paint dripping down a wall under the flow of gravity. Such systems are known to have instabilities, namely, the classic fingering instability that causes the paint to drip rather than flowing as a uniform front (7). This mechanism is the same one that leads to the formation of tears of wine (Fig. 1*A*), in which the driving mechanism is a Marangoni stress caused by a gradient in surface tension that is due to a gradient in the alcohol concentration in the meniscus on the wineglass because of differential evaporation of the alcohol (8–10).

To have an undercompressive shock in a 1D scalar conservation law, one needs two ingredients: (*i*) a nonconvex flux f for the bulk flow and (*ii*) some kind of higher order physics in the shock layer such as surface tension. The nonconvex flux typically results from two competing physical effects in the driving mechanism, for example, a surface stress and a bulk force in opposite directions. In the case of ion-bombarded surfaces, the nonconvexity is in the yield function. For both fluid films and ion-bombarded surfaces, the physics in the shock layer comes from surface tension or surface energies, resulting in a mathematical model with fourth-order diffusion. For such systems, undercompressive shocks are not generic. For weak shocks, in which the values u_L and u_R are close together, one expects a compressive shock even with fourth-order, rather than second-order, diffusion. The tears of wine example and the paint dripping example both correspond to this case. Undercompressive shocks can occur when the jump reaches a threshold and crosses a change in convexity of the flux. Moreover, undercompressive shocks do not exist for a finite range of parameters u_L and u_R; the theory predicts that for a given right state u_R, there is an isolated value of u_L for the undercompressive wave. This constraint means that such shockwaves are often accompanied by a companion wave in the form of a compressive shock or rarefaction fan to transition to the background material. It also means that any driving mechanism for undercompressive waves will trigger a specific wave with a known prescribed jump across the shock.

Another feature of compressive waves in driven films is that they tend to be unstable to transverse perturbations. The capillary ridge caused by surface tension is unstable to a beading effect, leading to paint dripping or instabilities in spin coating at high rotation speeds. These drips need to be controlled in any kind of design manufacturing process. One exciting aspect of the initial discovery of undercompressive shocks in thin films was their stability to transverse perturbations, thus creating a new stability mechanism for a driven coating process. However, that idea has not led, to date, to a stable design procedure for liquid-coating processes. There are other examples of undercompressive shocks in coating flows, including a very commonly observed phenomenon of water being pushed up the windshield of the car by the surface stress of the wind counterbalanced by gravity. Such behavior is potentially relevant to important applications like deicing of airplane wings (11).

In a study by Holmes-Cerfon et al. (12), it was proposed that two undercompressive waves could be collided to form isolated steep ridges. A fully 2D experiment was realized in a magnesium alloy under uniform irradiation by a focused ion beam. The results

compared well with fully 2D simulations of the nonlinear model (13). In the article by Perkinson et al. (1), the authors show that this design principle can be used to solve an inverse problem; given a prescribed desired end state with connected ridges, they successfully used the undercompressive waves to carve out the desired pattern. To solve the inverse problem, a 1D nonlinear model, in the form of a diffusive Hamilton–Jacobi equation, was developed for the nonlinear motion of the undercompressive ridge as it evolves. Monte Carlo simulations were carried out to identify the best choice of initial pit to create the final state using ion bombardment. The low-dimensional evolution model for the transverse motion of the shock was instrumental in solving this inverse problem because it allows for a lower dimensional set space of initial configurations for testing. This new work shows that such unusual wave patterns can be used to control design features in small-scale materials applications. Moreover, Perkinson et al. (1) present a new mathematical analysis that leads to a simplified 1D model that accurately describes the fully 2D motion of the front, a crucial feature needed to use undercompressive waves for design. This work has ramifications for both technological design procedures and new simplified model development for 2D effects in nonlinear wave propagation.

Acknowledgments

This work was supported by the US National Science Foundation under Grant DMS-1312543.

1 Perkinson JC, Aziz MJ, Brenner MP, Holmes-Cerfon M (2016) Designing steep, sharp patterns on uniformly ion-bombarded surfaces. *Proc Natl Acad Sci USA* 113:11425–11430.
2 Lighthill MJ, Whitham GB (1995) On kinematic waves II: A theory of traffic flow on long, crowded roads. *Proc R Soc Lond A Math Phys Sci* 229:317–345.
3 Richards PI (1956) Shock waves on the highway. *Oper Res* 4:42–51.
4 Chen HH, et al. (2005) Shocks in ion sputtering sharpen steep surface features. *Science* 310(5746):294–297.
5 Jacobs D, McKinney B, Shearer M (1995) Traveling wave solutions of the modified Korteweg-deVries-Burgers equation. *J Differ Equ* 116(2):448–467.
6 Bertozzi AL, Munch A, Fanton A, Cazabat AM (1998) Contact line stability and 'undercompressive shocks' in driven thin film flow. *Phys Rev Lett* 81(23):5169–5l72.
7 Huppert HE (1982) Flow and instability of a viscous current down a slope. *Nature* 300:427–429.
8 Fournier JB, Cazabat AM (1992) Tears of wine. *Europhys Lett* 20(6):517–522.
9 Hosoi A, Bush JWM (2001) Evaporative instabilities in climbing films. *J Fluid Mech* 442:217–239.
10 Venerus DC, Nieto Simavilla D (2015) Tears of wine: New insights on an old phenomenon. *Sci Rep* 5:16162.
11 Myers TJ, Charpin PF, Chapman SJ (2002) The flow and solidification of a thin fluid film on an arbitrary three-dimensional surface. *Phys Fluids* 14:2788–2803.
12 Holmes-Cerfon M, Aziz MJ, Brenner MP (2012) Creating sharp features by colliding shocks on uniformly irradiated surfaces. *Phys Rev B* 85:165441.
13 Holmes-Cerfon M, Zhou W, Bertozzi AL, Brenner MP, Aziz MJ (2012) Development of knife-edge ridges on ion-bombarded surfaces. *Appl Phys Lett* 101:143109.
14 Bowen M, Sur J, Bertozzi AL, Behringer RP (2005) Nonlinear dynamics of two-dimensional undercompressive shocks. *J Phys D Appl Phys* 209(1-4):36–48.